Controlled Formation and Characterization of Dithiothreitol-Conjugated Gold Nanoparticle Clusters

De-Hao Tsai,[†,⊥] Tae Joon Cho,[†] Frank W. DelRio,[†] Justin M. Gorham,[†] Jiwen Zheng,[§] Jiaojie Tan,[†,∥] Michael R. Zachariah,[‡,∥] and Vincent A. Hackley*,[†]

[†]Materials Measurement Science Division and [‡]Chemical Sciences Division, National Institute of Standards and Technology, Gaithersburg, Maryland 20899, United States

[§]Center for Devices and Radiological Health, Food and Drug Administration, Silver Spring, Maryland 20993, United States

[∥]Departments of Chemical Engineering and Chemistry, University of Maryland, College Park, Maryland 20740, United States

S *Supporting Information*

ABSTRACT: We report a systematic study of the controlled formation of discrete-sized gold nanoparticle clusters (GNCs) by interaction with the reducing agent dithiothreitol (DTT). Asymmetric-flow field flow fractionation and electrospray differential mobility analysis were employed complementarily to determine the particle size distributions of DTT-conjugated GNCs (DTT−GNCs). Transmission electron microscopy was used to provide visualization of DTT−GNCs at different states of aggregation. Surface packing density of DTT and the corresponding molecular conformation on the Au surface were characterized by inductively coupled plasma mass spectrometry and X-ray photoelectron spectroscopy. Results show that DTT increases the aggregation rate of gold nanoparticles (AuNPs) up to ≈100 times. A mixed conformation (i.e., combining vertically aligned, horizontally aligned, and cross-linking modes) exists for DTT on the Au surface for all conditions examined. The primary size of AuNPs, concentration of DTT, and the starting concentration of AuNPs influence the degree of aggregation for DTT−GNCs, indicating that the collision frequency, energy barrier, and surface density of DTT are the key factors that control the aggregation rate. DTT−GNCs exhibit improved structural stability compared to the citrate-stabilized GNCs (i.e., unconjugated) following reaction with thiolated polyethylene glycol (SH-PEG), indicating that cross-linking and surface protection by DTT suppresses disaggregation normally induced by the steric repulsion of SH-PEG. This work describes a prototype methodology to form ligand-conjugated GNCs with high-quality and well-controlled material properties.
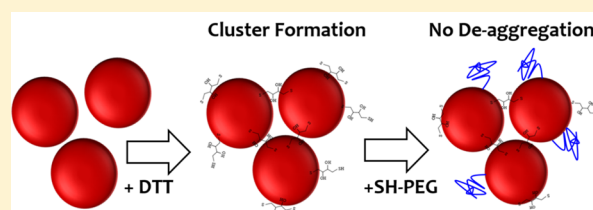
1. INTRODUCTION

Gold nanoparticle clusters (GNCs) are attractive for a variety of applications in nanotechnology and specifically bionano-technology.[1−12] The functional response is fundamentally governed by the interparticle coupling, especially the creation of electromagnetic hot spots by the coupling of surface plasmon resonance (SPR), which may lead to the magnification of optically allowed in-phase modes.[1,7−17] The SPR-enhancement of optical signals can be further improved by choosing suitable physical properties of GNCs, including the primary size of particle, dimensions, orientation, and interparticle spacing between primary particles.[1,8,9,13,14,17] With controlled size and dimension through assembly of gold nanoparticles (AuNPs), the discrete-sized GNCs (i.e., *n* < 5, where *n* is the number of primary particle per GNC) can be applied to the rational fabrication of nanoscale devices, including biodetection, bioimaging, and optoelectronic devices, with ultrahigh sensitivity.[3,4,6,9−12,15,18]

Surface functionalization via ligand conjugation is frequently utilized as a method to provide control over the physical properties of GNCs and also to enhance their functionality during the formation of GNCs.[5,6,9−12,15,16,19,20] Recent advances have been achieved in morphology-controlled synthesis of discrete-sized GNCs (i.e., dimers and trimers) using ligand conjugation. For example, Maye et al.,[16] Guo et al.,[6] and Park et al.[20] used DNA to functionalize the surface of AuNPs and to perform controlled aggregation with a designed interparticle spacing. Because of the ability to tailor surface chemistry, ligand conjugation by design provides the opportunity to form more defined GNCs.[2,9,11,12,16,20] Additionally, the binding between primary particles and the molecules present in the medium can be effectively controlled through the concept of surface functionalization, providing a route to enhance the structural stability of fabricated GNCs and thus prevent further aggregation or disaggregation.[19]

Although the physical (e.g., polydispersity, interparticle binding) and surface properties (e.g., state of charge, hydro-phobicity) of GNCs have been modified through surface modification via ligand conjugation, the quality of the resulting GNCs has been less than ideal.[2,9,11,13,21] An effective way to

Figure 1. Cartoon depiction of DTT conjugation on AuNPs: (A) cross-linking mode, (B) horizontally aligned mode, and (C) vertically aligned mode.

improve the homogeneity of discrete GNC species is to apply hydrodynamic fractionation following fabrication.[2,13] Chen et al.[2] and Tsai et al.[13] have demonstrated the use of density gradient centrifugation and asymmetric-flow field flow fractionation (A4F), respectively, in order to obtain dimeric or trimeric GNCs with a high degree of purity, yielding a substantial improvement (e.g., up to 90% purity for dimers). However, the size discrimination process may result in loss of a significant fraction of product, thus restricting the capacity for potential applications requiring, for example, gram quantities of purified product. Hence, understanding the mechanism that controls ligand-induced aggregation *prior* to size-classification is essential for improving formulation and yields of discrete-sized GNCs with desired properties (i.e., to maximize the population of selected materials prior to classification). This will be especially critical for colloidal systems characterized by a dynamic and unstable nature during the solution phase formation of size-controlled GNCs.

Our present objective is to develop a systematic methodology, including synthetic approaches and traceable characterization methods, to optimize the formation process of ligand-functionalized GNCs. We chose a suite of orthogonal measurement approaches, including A4F, electrospray differential mobility analysis (ES-DMA), transmission electron microscopy (TEM), X-ray photoelectron spectroscopy (XPS), and inductively coupled plasma mass spectrometry (ICP-MS), to provide a robust and comprehensive analysis of the formation process for functionalized GNCs. Dithiothreitol (DTT) was employed as the functional ligand. As shown in Figure 1, DTT has two thiol groups which can bond with Au in three ways:[22,23] bridging two AuNPs by forming a S−Au bond between each surface (cross-linking mode, Figure 1A), forming a dithiolate−Au bond (horizontally aligned mode, Figure 1B), or forming a single S−Au bond (vertically aligned mode, Figure 1C). The conformation of surface-bound DTT can be derived from the surface packing density (σ_{DTT}).[24] In comparison to van der Waals attraction for the unconjugated GNCs,[13,25] the energy for the interparticle DTT cross-linking (i.e., two S−Au bonds per DTT, >100 kJ/mol)[26−28] is expected to be higher, resulting in a more stable structure for DTT-conjugated GNCs (DTT−GNCs). Thiolated polyethylene glycol (SH-PEG) was chosen to test the structural integrity of as-formed GNCs; SH-PEG has been widely used to provide steric repulsion against aggregation and to mask drug delivery vectors to reduce renal clearance (thereby providing increased blood circulation time) in targeted drug delivery.[24,29−32] With the capacity to detect, control, and assess the physical and dimensional properties of GNCs simultaneously, one should be able to synthesize functional GNCs (e.g., dimers and trimers) with good structural stability (i.e., no disaggregation upon interactions with the ligands in the medium).

2. EXPERIMENTAL METHODS

2.1. Materials. Nominally 10, 30, and 60 nm citrate-stabilized monomodal colloidal AuNPs (denoted as 10AuNP, 30AuNP, and 60AuNP, respectively) were obtained from Ted Pella Inc. (Redding, CA).[33] Aqueous DTT (99%, Sigma-Aldrich, St. Louis, MO) concentration (C_{DTT}) ranged from 0.016 to 942 mmol/L. SH-PEG with a molecular mass of 1 kDa (SH-PEG1K) was obtained from Nanocs (New York, NY). Aqueous ammonium acetate (99.9%, Sigma-Aldrich) solution was prepared at pH 7 and 10−20 mmol/L and then used to adjust the ionic strength of samples and to perform electrospray ionization. Biological grade 18.2 MΩ·cm deionized (DI) water (Aqua Solutions, Jasper, GA) was used to prepare solutions and colloidal suspensions.

2.2. A4F. The A4F system consists of a high-performance liquid chromatography isocratic pump (1100 series, Agilent Technologies, Santa Clara, CA), manual injection valve (Rheodyne 7725i, IDEX Corp., Oak Harbor, WA) with a 100 μL stainless steel sample loop, field/flow control module and A4F separation channel (Eclipse 3+, Wyatt Technology), multiangle light scattering (MALS) detector (Dawn Heleos, Wyatt Technology), and ultraviolet−visible (UV−vis) absorbance diode array detector (1200 DAD, Agilent Technologies). The cross-flow rate was 2 mL/min and the channel flow was 0.5 mL/min. Details of the A4F method and operation have been described in our previous publications.[13,34] The particle size distributions measured by A4F were repeated at least once for each condition.

2.3. ES-DMA. The electrospray aerosol generator (ES) (model 3480, TSI Inc., Shoreview, MN) generates an aerosol using a fused silica capillary (40 μm inner diameter tip) directed into an electric field by a stream of dry air. The aerosolized AuNPs are delivered to the DMA (model 3080, TSI Inc.) with a sheath flow carrying the AuNPs downstream. The particles of a specific size are then counted using a condensation particle counter (CPC) (model 3776, TSI Inc.). A Bertan power supply (205B-10R, Valhalla, NY) is used to apply voltage to the DMA in our customized system. The electric field of the DMA and data acquisition for the CPC are controlled using a customized LabView program (National Instruments, Austin, TX). The ES-DMA-CPC was used to obtain a number-based particle size distribution. The step size used in the particle size measurements was 0.2 nm and the time interval between each step size was 10 s. Sheath flow rate (10 L/min) and sample flow rate (1 L/min) of the DMA were controlled by a mass flow controller (MKS Instruments, Andover, MA) and a customized laminar flow element (CME, Davenport, IA), respectively. Both argon and air were used as the sheath gas in the DMA. The resolution of the particle size measurements has been estimated previously at about 10% of the mean mobility size.[28,35,36]

2.4. XPS. XPS was performed on a Kratos Axis Ultra DLD spectrophotometer (Kratos Analytical, Manchester, UK) using an Al Kα monochromatic X-ray source at 150 W (10 mA, 15 kV) and a hemispherical analyzer located at the surface normal. The DTT−GNC samples were prepared on argon ion sputter cleaned silicon wafers by
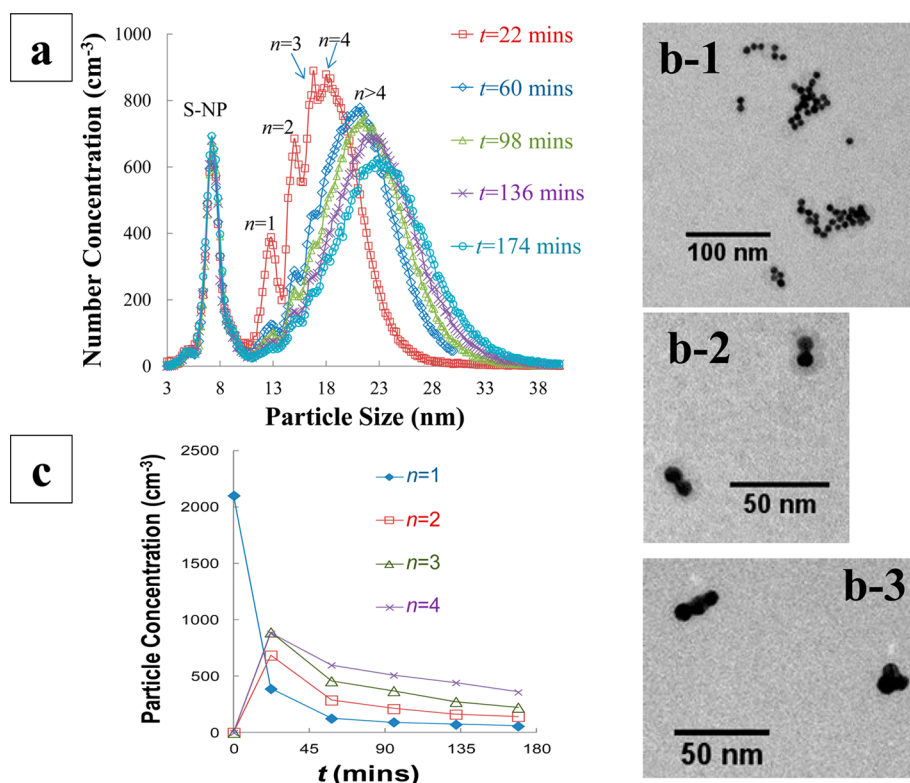
Figure 2. DTT-induced aggregation of AuNPs over time. Sample: 10AuNP. (a) PSDs measured by ES-DMA: squares, $t = 22$ min; diamonds, $t = 60$ min; triangles, $t = 98$ min; crosses, $t = 136$ min; circles, $t = 174$ min. (b) TEM images of DTT−GNCs: 1, without size-classification (collected right after all ES-DMA measurements, $t > 174$ min); 2, collected from peak $n = 2$; 3, collected from peak $n = 3$. The legend in part a gives the reaction time for each peak. (c) Change in number concentration of GNCs, $N_{p,n}$ versus t. $C_{DTT} = 0.94$ mmol/L. $N_{p,1,t=0} = 5.7 \times 10^{12}$ cm^{-3}. Ar was used as the sheath gas in the DMA measurements.

drop-casting a suspension and pumping down in a separate vacuum chamber overnight prior to introduction into ultrahigh vacuum (UHV) conditions ($P_{base} < 10^{-9}$ Torr). High-resolution spectra were acquired at a pass energy of 40 eV, with the hybrid lens and slot aperture with photoelectron intensity measured at 0.1 eV increments in triplicate for each sample analyzed. All data analysis was performed using CasaXPS software (Teignmouth, UK). All spectra were energy referenced to the Si (2p) photoelectron peak at 99.3 eV representative of zerovalent silicon.[37] As a result of interference from a silicon plasmon at approximately 168 eV, all S (2p) regions had the plasmon feature subtracted out of the spectra, on the basis of a control measurement from a clean Si wafer, prior to fitting with a Shirley background and peak-fitting. Thus, only qualitative variations in the S concentration have been reported.

2.5. ICP-MS. An ICP-MS (model 7700x, Agilent Technologies) was used to measure the mass fraction of Au and S using calibration curves generated from standard solutions. Details of experimental conditions are described in previous publications[24,35,36] and summarized in the Supporting Information (SI).

2.6. TEM. Particles for imaging were aerosolized and deposited onto a TEM grid with carbon film using an electrostatic aerosol sampler (model 3089, TSI Inc.). The deposition-induced aggregation can then be minimized due to the electrostatic repulsion between the deposited AuNPs and the to-be-deposited AuNPs.[25,28] The morphology and quality of deposited AuNPs were imaged using a JEM-1400 (JEOL Inc., Peabody, MA) at an acceleration voltage of 80 kV. Because of the low surface coverage, the GNC images were analyzed after using visual inspection to locate multiple areas on each sample.

2.7. Zeta Potential Analysis. The zeta potential of gold colloids was determined using a palladium dip cell with a Zetasizer Nano ZS (Malvern Instruments Inc.) and converted from the electrophoretic mobility using the Smoluchowski approximation.[38]

3. RESULTS AND DISCUSSION

3.1. Formation of DTT−GNCs. Figure 2a shows the particle size distribution (PSD) of 10AuNPs, after treatment with DTT. The concentration of DTT (C_{DTT}) was 0.94 mmol/L. To minimize the interference from the remnant particles induced by the drying process of electrospray-generated droplets (denoted as S-NP), all aerosolized particles were first transmitted through a tube furnace at $T = 300$ °C prior to size classification.[36] Several distinct peaks are apparent at a reaction time of $t = 22$ min, indicative of DTT−GNCs with different degrees of aggregation: mobility diameter ($d_{p,m}$) = 12.8 nm for monomers ($n = 1$), $d_{p,m} = 15.0$ nm for dimers ($n = 2$; determination of the peak size and conformation of GNCs are described in previous publications),[13,25] $d_{p,m} = 16.8$ nm for trimers ($n = 3$), and $d_{p,m} = 18$ nm for tetramers ($n = 4$). The peak size for DTT−GNCs was almost identical to the values of citrate-stabilized (i.e., unconjugated) GNCs,[28] indicating that the layer thickness of the DTT corona on the Au surface is negligible (i.e., below the resolution of DMA). As t increased, we found that the PSD was shifted toward larger sizes, where the peaks representing the discrete-sized GNCs (i.e., $n < 5$) became indistinguishable. Visual inspection showed that the corresponding AuNP solution had changed in appearance from ruby red ($t = 0$ min) to blue ($t > 85$ min). The colorimetric change (i.e., red-shift of AuNP plasmon bands)[39] confirmed the formation of GNCs, even though the aggregation state could not be discerned quantitatively by simple visual inspection.[13,25]

Microscopic methods confirmed the aggregation process induced by DTT. As shown in Figure 2b-1, we found that 10AuNPs aggregated significantly after interacting with DTT,
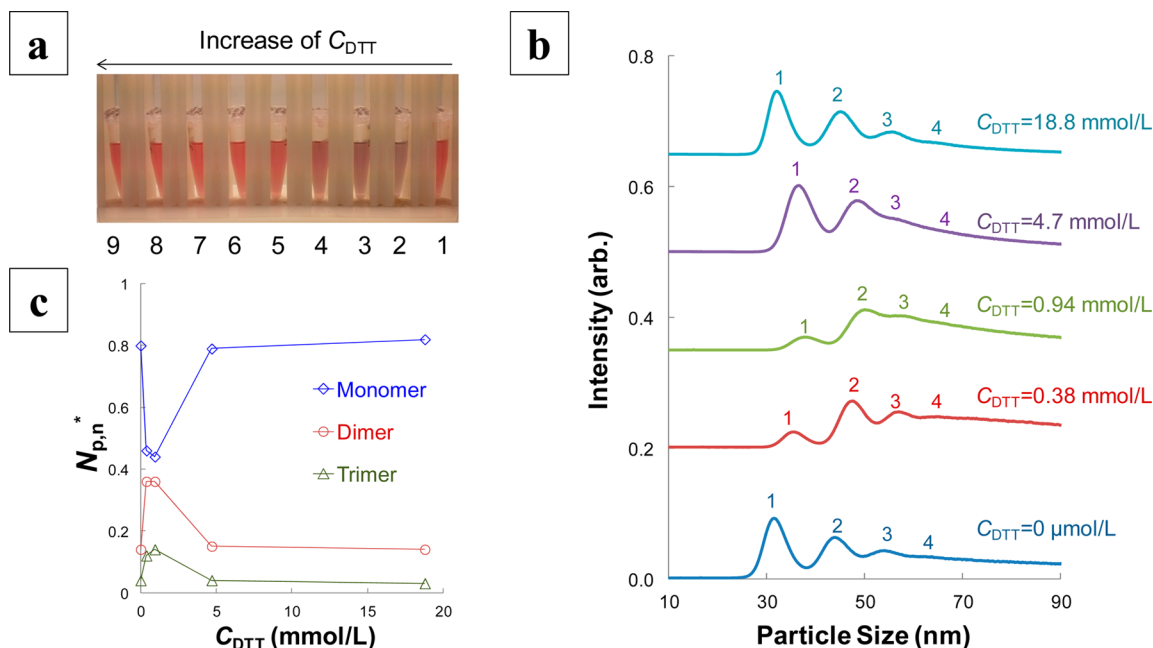
Figure 3. Effect of C_{DTT} on the formation of DTT−GNCs. Samples: 30AuNPs. (a) Visual appearance of 30AuNPs after treatment with DTT: 1, $C_{DTT} = 0$ mmol/L; 2, $C_{DTT} = 0.38$ mmol/L; 3, $C_{DTT} = 0.94$ mmol/L; 4, $C_{DTT} = 1.9$ mmol/L; 5, $C_{DTT} = 4.7$ mmol/L; 6, $C_{DTT} = 9.4$ mmol/L; 7, $C_{DTT} = 18.8$ mmol/L; 8, $C_{DTT} = 47.1$ mmol/L; 9, $C_{DTT} = 178.9$ mmol/L. (b) PSDs at various C_{DTT} measured by A4F coupled with MALS. (c) $N_{p,n}*$ versus C_{DTT}. $N_{p,1,t=0} = 2.0 \times 10^{11}$ cm^{-3}.

as compared to previous studies that reported only a small amount of aggregation for monodisperse 10AuNPs without DTT.[28] By collecting the NPs under conditions corresponding to the peaks shown in Figure 2a, we were able to confirm that peak 2, or the $n = 2$ fraction, contained mainly dimerized 10AuNPs (Figure 2b-2) and that peak 3, or the $n = 3$ fraction, contained mainly trimers (Figure 2b-3). It is important to point out that the size discrimination of DTT−GNCs decreases as the cluster size increases, mainly due to an increase in the complexity of the cluster conformation (i.e., the number of possible configurations increase with cluster size, leading to overlapping peaks).

Figure 2c summarizes the number concentration of DTT−GNCs in gas phase as a function of reaction time. The number concentration of monomers decreased drastically until $t = 58$ min. At the same time, the concentration of dimers, trimers, and tetramers reached a maximum at $t = 22$ min, and then continually decreased due to the formation of large-sized (nondiscrete) GNCs ($n > 4$). These results indicate that the aggregation process begins with depletion of monomers to form discrete-sized GNCs ($n = 2−4$),[25,35] and then the reaction mechanism transitions toward cluster−cluster interactions to form large-sized clusters or aggregates ($n > 4$). Note that the peak concentration representing $n = 4$ was chosen at $d_{p,m} = 18$ nm in Figure 2c.

We then calculated the aggregation rate constant for AuNPs, k_0, using the irreversible population balance equation attributed to the Smoluchowski model[25,40]

$$k_0 = \frac{1}{N_{p,1,t=0}t}\left(\frac{N_{p,1,t=0}}{N_{p,n,\text{total}}} - 1\right) \tag{1}$$

where $N_{p,n,\text{total}}$ is the total number concentration (i.e., of all particle populations) at time t and $N_{p,1,t=0}$ is the number concentration of primary AuNPs at $t = 0$ min (i.e., equal to the total starting concentration of particles). Using a linear fitting of

$N_{p,1,t=0}/N_{p,n,\text{total}}$ versus t for the 10AuNPs (see SI), one obtains $k_0 \approx 10^{-16}$ cm^3/s. Thus, the k_0 value here is ≈100 times larger than in the absence of DTT at the same ionic strength (further details on the derivation of k_0 are described in the SI). The results show that the presence of DTT enhances the rate of aggregation; further modifications to the aggregation rate via changes to C_{DTT}, primary particle size ($d_{p,1}$), and particle concentration ($N_{p,n}$) are investigated in the ensuing sections.

3.2. Effect of DTT Concentration on Formation of GNCs. We investigated the effect of C_{DTT} on the aggregation state of GNCs using 30AuNPs. Visual inspection (Figure 3a) shows a color change (i.e., becomes more purplish or red-shifted[39]) when C_{DTT} increases from 0 to 0.94 mmol/L. However, the colorimetric response reverses course (i.e., a blue-shift is observed) when C_{DTT} increases from 0.94 to 178.9 mmol/L. These results indicate that 30AuNPs had the highest level of aggregation when 0.38 mmol/L < C_{DTT} < 1.9 mmol/L.

To quantify the effect of aggregation as a function of C_{DTT}, we used A4F coupled with a MALS detector (using 90° angle) to measure the PSDs of GNCs in the solution phase. The advantage of A4F is the high sensitivity to detect the presence of a small quantity of clusters;[13] this should be especially useful when the population of discrete-sized GNCs is low during the early stage of aggregation.[13,25] A subset of the samples from Figure 3a were measured by A4F, as shown in Figure 3b, where several distinct bands were found to be present for all measured samples. The dominant species in each eluting peak has been identified using online-mode UV−vis:[13] monomers in peak 1, dimers in peak 2, trimers in peak 3, and a mixture of higher order species (especially tetramers) in peak 4 (actually a broad band). The peak size changed as a function of C_{DTT}. Since the species are the same and the coating thickness of DTT is negligible, the peak size differences are attributed to changes in retention behavior due to interactions with the A4F membrane
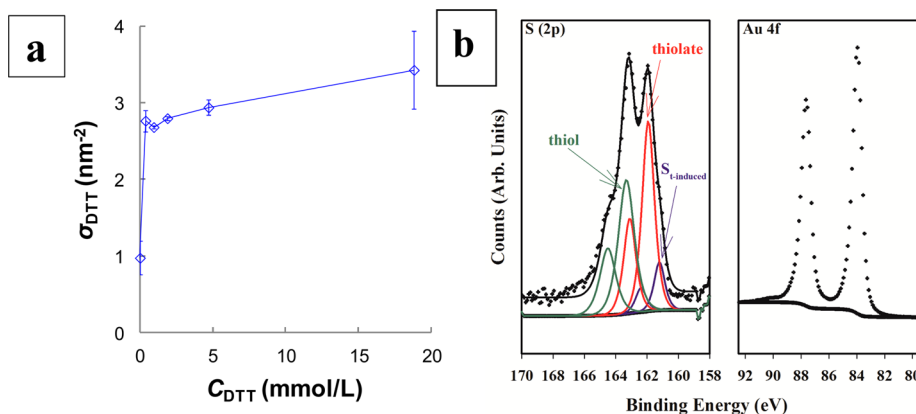
Figure 4. (a) Adsorption isotherm for DTT on 30AuNPs as measured by ICP-MS. Error bars and uncertainty intervals associated with reported (mean) measurement values represent one standard deviation calculated from (two to four) replicate measurements. (b) Fitted S (2p) and Au (4f) spectra of DTT-treated 30AuNPs measured by XPS. $C_{DTT} = 0.38$ mmol/L.

(accumulation wall), and not the thickness of the DTT corona itself.

On the basis of the results from Figure 3b, we can convert the scattering intensity of each peak measured by the MALS detector into $N_{p,n}$, and the corresponding number ratio in a population, $N_{p,n}*$ by[13]

$$N_{p,n}* = \frac{N_{p,n}}{\sum_{n=1}^{4} N_{p,n}} = \frac{I_{p,n}}{n^2 V_{p,n=1}^2} \qquad (2)$$

where $I_{p,n}$ is the scattered intensity for GNCs containing n monomers, $V_{p,n=1}$ is the volume of a singlet (monomer) AuNP (assuming spherical geometry).[13] Figure 3c shows $N_{p,n}*$ of monomers, dimers, and trimers as a function of C_{DTT}. We observe that the monomer concentration reaches a minimum at 0.4 mmol/L < C_{DTT} < 1 mmol/L, and the monomer fraction is relatively constant above this range. The formation of dimers and trimers exhibits the opposite trend, reaching a maximum at 0.4 mmol/L < C_{DTT} < 1 mmol/L. This result suggests an operational window to optimize the synthesis of dimeric and trimeric GNCs: $C_{DTT} = 0.4-1$ mmol/L.

On the basis of classical Derjaguin−Landau−Verwey−Overbeek (DLVO) theory,[41] the long-range electrostatic repulsion and the short-range van der Waals attraction are considered the key factors in the stability of colloidal suspensions. The electrostatic interaction of DTT−GNCs over various C_{DTT} can be estimated on the basis of their zeta potentials (ψ_z), which ranged from ≈ −18 to −27 mV and were relatively insensitive to C_{DTT}: $\psi_z = -18.2 \pm 1.1$ mV at $C_{DTT} = 0$ mmol/L; $\psi_z = -21.0 \pm 1.3$ mV at $C_{DTT} = 0.38$ mmol/L; $\psi_z = -27.1 \pm 1.5$ mV at $C_{DTT} = 0.94$ mmol/L; $\psi_z = -23.4 \pm 1.1$ mV at $C_{DTT} = 18.8$ mmol/L. Hence, the differences in the aggregation states as a function of C_{DTT} cannot be explained simply by changes in electrostatic repulsion. Similarly, van der Waals attractive forces are not affected by the presence of DTT conjugation, as this is principally determined by the Au core composition and size. It is feasible that DTT contributes to an increase in the sticking efficiency during particle collisions, due to dangling (unbound) thiol groups; the relatively low zeta potential would increase the likelihood of close encounters. Note that both the effects of ionic strength and pH toward colloidal stability are negligible in our study, since the pH value and the salt concentration of our sample solutions are constant (i.e., 10 mmol/L ammonium acetate aqueous solution at pH 7).

To investigate the possible short-range interactions induced by DTT, we used ICP-MS to characterize the surface packing density and corresponding conformation of DTT on Au. Figure 4a shows the adsorption isotherm of DTT on 30AuNPs as measured by ICP-MS. The maximum σ_{DTT} on the AuNP surface ($\sigma_{DTT,max}$) is ≈3.2 nm^{-2}, or about 50% of the theoretical maximum density for a short-chain self-assembled mono-layer.[31,42] By correlating the aggregation state with σ_{DTT}, we can show that aggregation is higher at lower σ_{DTT} (≈ 2.8 nm^{-2}). In other words, when there is substantial unreacted Au surface available, the patchiness of the particles leads to more rapid aggregation.

As depicted in Figure 1, the likely conformation of surface-bound DTT will be impacted by σ_{DTT}.[24] At low σ_{DTT}, DTT can cross-link between two individual AuNPs (Figure 1a) or form two S−Au bonds on the surface of an individual AuNP (Figure 1b),[24] until surface saturation is reached. Hence, the cross-linking and horizontally aligned modes of DTT adsorption are more likely when C_{DTT} < 1 mmol/L.

The XPS results provide information regarding the local chemical environment of the S from the DTT and the Au from the AuNPs. Figure 4b shows different functionalities within the S (2p) region identified as a thiol (S−H) at ≈163.2 eV, thiolate (S−Au) at ≈162.0 eV,[43] and $S_{t-induced}$ component (analysis time induced) at ≈161.1 eV acquired from the first of a series of three XPS measurements on a given sample as well as the Au (4f) region at ≈83.9 eV, typical of zerovalent gold. From the spectra, one can see that the dominant component from the first scan is a thiolate functionality, suggesting that a Au−S bond has been formed. A secondary component is the unbound thiol functionality, which could result from excess DTT or from DTT binding solely through one S−Au bond. While the identity of the $S_{t-induced}$ species is unclear, the peak does increase with increasing analysis time and exposure to X-rays (as shown in SI, Figure S6) as was observed for three separate DTT−Au samples, each with XPS spectra acquired in triplicate. While this binding energy regime is most comparable to sulfide species,[44] we have not found evidence of a negative shift in binding energy due to X-ray exposure of a thiol, and therefore, the species will only be stated to be time-induced. XPS results indicate DTT may likely form a disordered layer on the surface of AuNPs of some combination of all three modes depicted in Figure 1. However, the XPS results cannot distinguish between thiolates in the various modes.
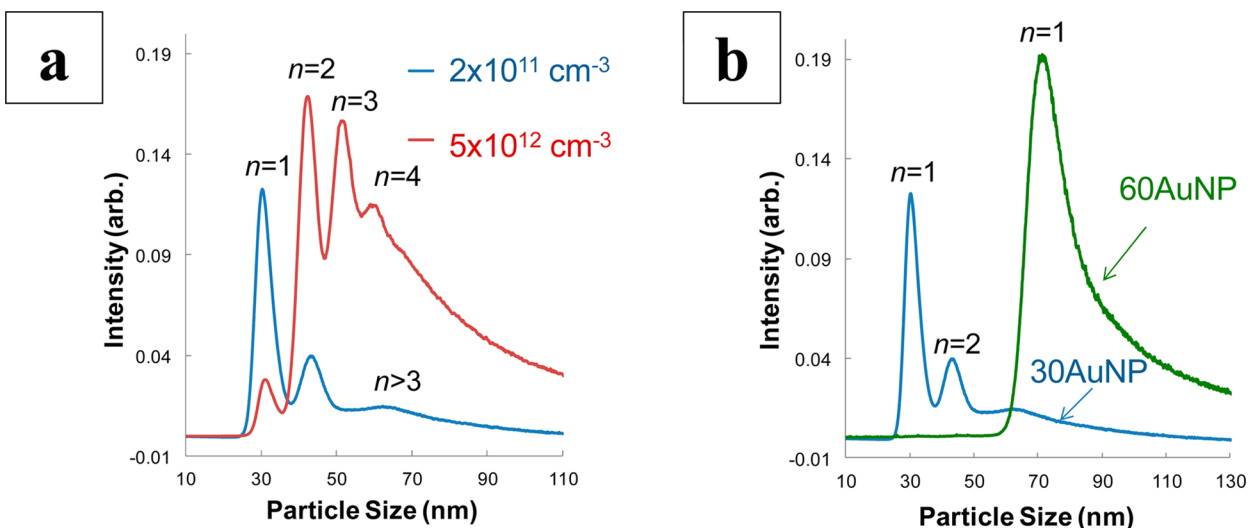
Figure 5. Effects of particle number concentration and primary size of AuNPs on the aggregation state of GNCs after 5-day reaction: (a) 30AuNPs as measured by A4F at $N_{p,1,t=0} = 2 \times 10^{11}$ cm^{-3} and $N_{p,1,t=0} = 5 \times 10^{12}$ cm^{-3} and (b) 30AuNP compared to 60AuNPs with $N_{p,1,t=0} = 2 \times 10^{11}$ cm^{-3}.
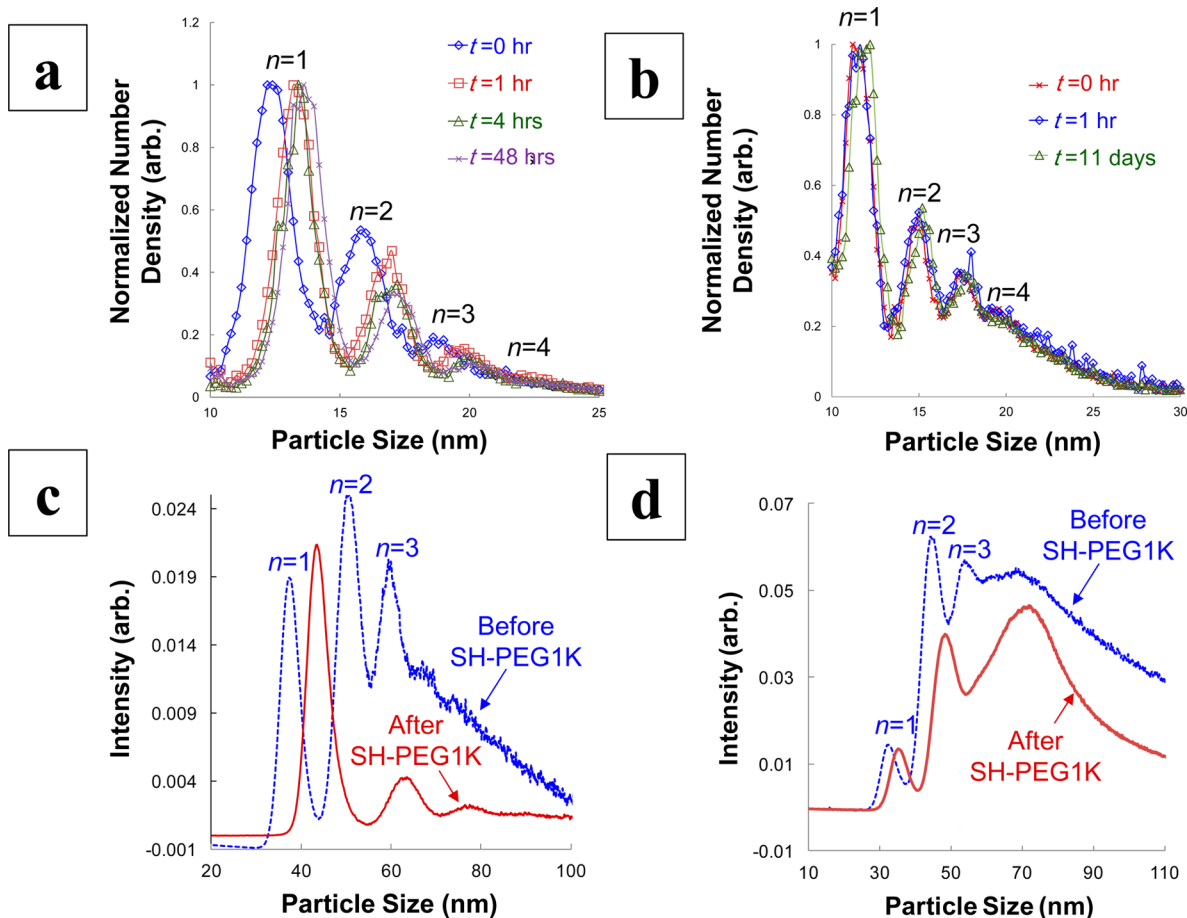
Figure 6. Effect of SH-PEG1K interaction on GNCs. (a) PSDs of unconjugated GNCs measured by ES-DMA. Sample: 10AuNP. (b) PSDs of DTT−GNCs measured by ES-DMA. Sample: 10AuNP. (c) PSDs of unconjugated GNCs measured by A4F. Sample: 30AuNP. (d) PSDs of DTT− GNCs measured by A4F. Sample: 30AuNP. Air was used as the sheath gas in DMA measurements.

3.3. Effect of Starting Concentration and Primary Particle Size on Formation of GNCs. Although the particle collision rate (frequency) scales with the square of the particle concentration,[25,40] not every collision necessarily results in sticking. In the case of DTT-induced aggregation, the process may be reaction-limited (i.e., not limited by Brownian kinetics, but by the stickiness or reactivity during collisions). Regardless, by increasing the particle concentration, the number of collisions per unit time should increase, and thus, the rate will increase, that is, unless the stickiness is extremely low. For 30AuNPs, as shown in Figure 5a, by increasing $N_{p,1,t=0}$ a factor of 25, the degree of aggregation increases: the peak intensities

of dimers (peak 2), trimers (peak 3), and tetramers (peak 4) increase significantly, with a decrease in the monomer intensity (peak 1), following a 5-day reaction period. Assuming only discrete-sized GNCs present in the system (i.e., $n < 5$), the total number of particles present is estimated to decrease 29%, yielding a 2.3 times increase in k_0. The results indicate that DTT-induced aggregation is proportional to the collision frequency of particles, which is consistent with a relatively moderate energy barrier to collision (i.e., in the intermediate regime)[13,25] and a relatively high reactivity (not truly reaction-limited; a theoretical calculation of the energy barrier is summarized in the SI). In addition to collision frequency, increasing $N_{p,n,t=0}$ may also affect the number of available sites on the AuNP surface to allow DTT adsorption. Even though C_{DTT} is at least 5 times greater than the saturation level, it is still plausible that the cross-linking and horizontally aligned modes are formed at a higher $N_{p,n,t=0}$ (i.e., more available sites to bind), resulting in an increase of aggregation.

Figure 5b compares the A4F elution trace for 60AuNPs with that of 30AuNPs under identical reaction conditions after a 5-day period ($N_{p,n,t=0} = 2 \times 10^{11}$ cm^{-3} and $C_{DTT} = 377$ μmol/L). In contrast to 30AuNPs, the formation of GNCs was not obvious for the larger 60AuNPs. We also examined the 10AuNPs under the same conditions and found that 30AuNPs are less aggregated; however, in this case aggregation of 10AuNPs is so rapid and severe that discrete GNCs cannot be determined by A4F after 5 days. The reason for the apparent size dependency on the aggregation rate could be explained by the difference in the energy barrier against aggregation, since the energy barrier has been shown to be proportional to $d_{p,1}$ in the intermediate regime (e.g., the energy barrier of 60AuNP is ≈ 2 times higher than that of 30AuNP).[25] Hence, GNCs with a smaller primary size have a higher aggregation rate. Note that the C_{DTT} was at least 30 times greater than the saturation level in Figure 5b. Also, the ratio of total surface area to ligand concentration is varied due to differences in the total Au surface area (e.g., the surface area of 60AuNP is ≈ 4 times higher than the area of 30AuNP shown in Figure 5b), which might result in different DTT-binding conformations with the subsequent impact on aggregation rate for these samples.

3.4. Effect of SH-PEG1K on the Structural Stability of DTT−GNCs. Though it is assumed that the aggregation of AuNPs is irreversible due to the strong interparticle binding from van der Waals forces,[13,25] the binding affinity within a GNC can be changed once its surface has been modified by binding ligands. SH-PEG1K was chosen to test the structural stability of DTT−GNCs. As previously demonstrated,[29,31] surface functionalization with SH-PEG can be used to reduce the binding affinity between Au surfaces. In comparison to other types of binding ligands, such as citrate ions, the long chain, hydrophilic SH-PEG has shown its effectiveness and provides the necessary stability against aggregation.[24,31] Recently, Schultz et al.[45] and Stewart et al.[46] reported surface modification with SH-PEG to improve the colloidal stability of AuNPs against DTT-induced aggregation.[45,46] On the other hand, for the prospect of structural stability of GNCs, once SH-PEG is bound to the surface of Au, the reduction of interparticle binding could induce disaggregation of GNCs (i.e., the steric repulsion by SH-PEG1K overcomes the sum of attractive forces within a GNC).

Figure 6 shows the PSDs of GNCs measured by ES-DMA over time, following interacting with SH-PEG1K. The concentration of SH-PEG1K used was 20 μmol/L. For GNCs without DTT (i.e., only citrate-stabilized, where cluster formation was induced via electrostatic screening by ammonium acetate, Figure 6a), the peak size of unconjugated GNCs increased by 1 nm (for $n = 1-4$), indicating the adsorption of SH-PEG on the GNCs. Then, unconjugated GNCs obviously disaggregated over time, possibly due to the repulsion between the surface-conjugated SH-PEG1K. Additionally, the number density increased with exposure time to the SH-PEG1K. This may be a result of deaggregation of larger agglomerates and higher transport efficiency related to the SH-PEG-functionalized GNCs. As a result, the relative ratios were employed to compare and contrast the impact of adding SH-PEG1K. Indeed, after a 48 h reaction (purple crosses, Figure 6a), the ratios of monomers to dimers and trimers increased by $\approx 39\%$ and $\approx 47\%$, respectively, confirming that unconjugated GNCs are not stable in the presence of SH-PEG. In comparison, the DTT−GNC PSDs did not exhibit any significant changes, even after an 11 day reaction with SH-PEG1K (green triangles, Figure 6b. $C_{DTT} = 18.8$ mmol/L); the peak sizes for $n = 1$ to $n = 4$ remain similar to the condition without SH-PEG1K (red crosses, Figure 6b). The results show DTT−GNCs remain stable even after the interaction with SH-PEG. Additionally, the nominal peak size of each population increases more for citrate-stabilized AuNPs than for DTT treated AuNPs, suggesting that SH-PEG1K was taken up more readily on the citrate-stabilized GNCs. A4F results confirm that DTT−GNCs (Figure 6d) supports better structural stability relative to citrate stabilized GNCs (Figure 6c). The increase in peak size for $n = 1$ and 2 confirms the adsorption of SH-PEG1K in both cases. Since the disaggregation of GNCs was induced by ligand exchange-type competitive adsorption between the surface-bound DTT and the unbound SH-PEG1K, the rate of disaggregation should be proportional to the concentration of SH-PEG1K and inversely proportional to the concentrations of unbound DTT and AuNPs. We found that sample recovery during A4F analysis was affected by the surface interaction of GNCs with the membrane, thus making direct comparisons of peak area for the different populations over time less rigorous (e.g., lower recovery of DTT−GNCs with SH-PEG1K was observed in this study). Note that 30AuNP samples were used for A4F measurements, and 10AuNP samples were used for ES-DMA measurements. Number densities shown in Figure 6a,b were normalized against the number density of the monomer peak ($n = 1$).

Figure 7 shows a cartoon depiction to demonstrate the possible interactions between SH-PEG1K and GNCs (Figure 6). Without DTT conjugation (Figure 7a), SH-PEG1K may adsorb to the surface of Au to provide steric repulsion against the interparticle binding via van der Waals forces, resulting in disaggregation of GNCs once the SH-PEG packing density is sufficiently high. In comparison, the presence of DTT improves the GNCs stabilization, presumably via thiolate bridging and the reduction of SH-PEG adsorption;[24,31] the surface-bound SH-PEG is incapable of separating bound particles due to the limited steric repulsion. However, due to the nature of ligand displacement,[24,30,31] it is possible that the DTT−GNCs may still disaggregate over a longer period of time, if the equilibrium concentration of SH-PEG1K is significantly higher than C_{DTT} in the solution phase.

4. CONCLUSIONS

DTT can be used to synthesize discrete-sized GNCs, and the mechanism of DTT-induced aggregation can be derived using
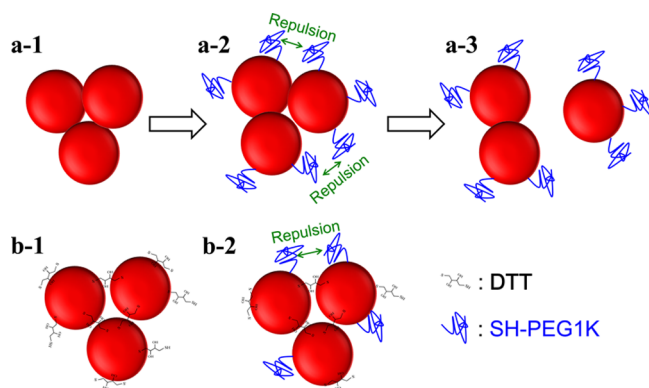
Figure 7. Cartoon depiction of SH-PEG1K interaction with GNCs. (a) Unconjugated GNCs (1) before interaction with SH-PEG1K, (2) upon SH-PEG1K conjugation, and (3) disaggregation of GNCs due to the repulsion of surface-bound SH-PEG1K. (b) DTT−GNCs (1) before interaction with SH-PEG1K and (2) upon SH-PEG1K conjugation.

complementary physical, microscopic, and spectroscopic approaches. The aggregation rate is dictated by C_{DTT}, as well as starting particle concentration and primary particle size. Due to the increased likelihood of cross-linking and horizontally aligned conformation of surface-bound DTT, DTT−GNCs with a lower molecular packing density (i.e., relatively low C_{DTT}) have a higher aggregation rate. Samples with a smaller primary size (e.g., 10AuNP in our experiments) exhibit an increased sticking efficiency and thus faster aggregation kinetics, because of a smaller energy barrier. The aggregation rate is proportional to the collision frequency, which in turn increases with the particle concentration. Through interparticle cross-linking via thiolate bridging, DTT−GNCs demonstrate an improved structural stability in the presence of other binding ligands in the system (e.g., SH-PEG1K). The prototype methodology we demonstrate here can be applied to the synthesis of other types of functionalized nanoparticle clusters (e.g., DNA-stranded GNCs, dumbbell-type nanoparticle clusters).

■ ASSOCIATED CONTENT

S **Supporting Information**

ICP-MS measurement conditions, additional TEM images of DTT conjugated GNCs, derivation and graphical determination of aggregation rate constants, depiction of GNC structures, detailed XPS results, and calculation of energy barrier as a function of particle size. This material is available free of charge via the Internet at http://pubs.acs.org/.

■ AUTHOR INFORMATION

Corresponding Author

*E-mail: vince.hackley@nist.gov. Phone: 301-975-5790. Fax: 301-975-5334.

Present Address

[1]Department of Chemical Engineering, National Tsing Hua University, Hsinchu, Taiwan, R.O.C.

Notes

The authors declare no competing financial interest.

■ ACKNOWLEDGMENTS

■ REFERENCES

(1) Hu, Y. X.; Sun, Y. G. A Generic Approach for the Synthesis of Dimer Nanoclusters and Asymmetric Nanoassemblies. *J. Am. Chem. Soc.* **2013**, *135*, 2213−2221.

(2) Chen, G.; Wang, Y.; Tan, L. H.; Yang, M. X.; Tan, L. S.; Chen, Y.; Chen, H. Y. High-Purity Separation of Gold Nanoparticle Dimers and Trimers. *J. Am. Chem. Soc.* **2009**, *131*, 4218−4219.

(3) Yuan, H.; Register, J. K.; Wang, H. N.; Fales, A. M.; Liu, Y.; Vo-Dinh, T. Plasmonic Nanoprobes for Intracellular Sensing and Imaging. *Anal. Bioanal. Chem.* **2013**, *405*, 6165−6180.

(4) Mangelson, B. F.; Park, D. J.; Ku, J. C.; Osberg, K. D.; Schatz, G. C.; Mirkin, C. A. Tunable and Broadband Plasmonic Absorption via Dispersible Nanoantennas with Sub-10 nm Gaps. *Small* **2013**, *9*, 2250−2254.

(5) Lan, X.; Chen, Z.; Liu, B. J.; Ren, B.; Henzie, J.; Wang, Q. B. DNA-Directed Gold Nanodimers with Tunable Sizes and Interparticle Distances and Their Surface Plasmonic Properties. *Small* **2013**, *9*, 2308−2315.

(6) Guo, L. H.; Xu, Y.; Ferhan, A. R.; Chen, G. N.; Kim, D. H. Oriented Gold Nanoparticle Aggregation for Colorimetric Sensors with Surprisingly High Analytical Figures of Merit. *J. Am. Chem. Soc.* **2013**, *135*, 12338−12345.

(7) Yang, X. P.; Su, Y.; Paau, M. C.; Choi, M. M. F. Mass Spectrometric Identification of Water-Soluble Gold Nanocluster Fractions from Sequential Size-Selective Precipitation. *Anal. Chem.* **2012**, *84*, 1765−1771.

(8) Gwo, S.; Lin, M. H.; He, C. L.; Chen, H. Y.; Teranishi, T. Bottom-Up Assembly of Colloidal Gold and Silver Nanostructures for Designable Plasmonic Structures and Metamaterials. *Langmuir* **2012**, *28*, 8902−8908.

(9) Romo-Herrera, J. M.; Alvarez-Puebla, R. A.; Liz-Marzan, L. M. Controlled Assembly of Plasmonic Colloidal Nanoparticle Clusters. *Nanoscale* **2011**, *3*, 1304−1315.

(10) Novak, J. P.; Feldheim, D. L. Assembly of Phenylacetylene-Bridged Silver and Gold Nanoparticle Arrays. *J. Am. Chem. Soc.* **2000**, *122*, 3979−3980.

(11) Chen, G.; Wang, Y.; Yang, M. X.; Xu, J.; Goh, S. J.; Pan, M.; Chen, H. Y. Measuring Ensemble-Averaged Surface-Enhanced Raman Scattering in the Hotspots of Colloidal Nanoparticle Dimers and Trimers. *J. Am. Chem. Soc.* **2010**, *132*, 3644−3645.

(12) Cheng, L.; Song, J. B.; Yin, J.; Duan, H. W. Self-Assembled Plasmonic Dimers of Amphiphilic Gold Nanocrystals. *J. Phys. Chem. Lett.* **2011**, *2*, 2258−2262.

(13) Tsai, D. H.; Cho, T. J.; DelRio, F. W.; Taurozzi, J.; Zachariah, M. R.; Hackley, V. A. Hydrodynamic Fractionation of Finite Size Gold Nanoparticle Clusters. *J. Am. Chem. Soc.* **2011**, *133*, 8884−8887.

(14) Hung, L.; Lee, S. Y.; McGovern, O.; Rabin, O.; Mayergoyz, I. Calculation and Measurement of Radiation Corrections for Plasmon Resonances in Nanoparticles. *Phys. Rev. B* **2013**, *88*.

(15) Chen, J. I. L.; Chen, Y.; Ginger, D. S. Plasmonic Nanoparticle Dimers for Optical Sensing of DNA in Complex Media. *J. Am. Chem. Soc.* **2010**, *132*, 9600−9601.

(16) Maye, M. M.; Nykypanchuk, D.; Cuisinier, M.; van der Lelie, D.; Gang, O. Stepwise Surface Encoding for High-Throughput Assembly of Nanoclusters. *Nat. Mater.* **2009**, *8*, 388−391.

(17) Peng, S.; Lei, C. H.; Ren, Y.; Cook, R. E.; Sun, Y. G. Plasmonic/Magnetic Bifunctional Nanoparticles. *Angew. Chem. Int. Ed.* **2011**, *50*, 3158−3163.

(18) West, J. L.; Halas, N. J. Engineered Nanomaterials for Biophotonics Applications: Improving Sensing, Imaging, and Therapeutics. *Annu. Rev. Biomed. Eng.* **2003**, *5*, 285−292.

(19) Wang, X. J.; Li, G. P.; Chen, T.; Yang, M. X.; Zhang, Z.; Wu, T.; Chen, H. Y. Polymer-Encapsulated Gold-Nanoparticle Dimers: Facile

Preparation and Catalytical Application in Guided Growth of Dimeric ZnO-Nanowires. *Nano Lett.* **2008**, *8*, 2643–2647.

(20) Park, S. Y.; Lytton-Jean, A. K. R.; Lee, B.; Weigand, S.; Schatz, G. C.; Mirkin, C. A. DNA-Programmable Nanoparticle Crystallization. *Nature* **2008**, *451*, 553–556.

(21) Zook, J. M.; Rastogi, V.; MacCuspie, R. I.; Keene, A. M.; Fagan, J. Measuring Agglomerate Size Distribution and Dependence of Localized Surface Plasmon Resonance Absorbance on Gold Nanoparticle Agglomerate Size Using Analytical Ultracentrifugation. *ACS Nano* **2011**, *5*, 8070–8079.

(22) Creczynski-Pasa, T. B.; Millone, M. A. D.; Munford, M. L.; de Lima, V. R.; Vieira, T. O.; Benitez, G. A.; Pasa, A. A.; Salvarezza, R. C.; Vela, M. E. Self-assembled Dithiothreitol on Au Surfaces for Biological Applications: Phospholipid Bilayer Formation. *Phys. Chem. Chem. Phys.* **2009**, *11*, 1077–1084.

(23) MacDairmid, A. R.; Gallagher, M. C.; Banks, J. T. Structure of Dithiothreitol Monolayers on Au(111). *J. Phys. Chem. B* **2003**, *107*, 9789–9792.

(24) Tsai, D. H.; Shelton, M. P.; DelRio, F. W.; Elzey, S.; Guha, S.; Zachariah, M. R.; Hackley, V. A. Quantifying Dithiothreitol Displacement of Functional Ligands from Gold Nanoparticles. *Anal. Bioanal. Chem.* **2012**, *404*, 3015–3023.

(25) Tsai, D. H.; Pease, L. F., 3rd; Zangmeister, R. A.; Tarlov, M. J.; Zachariah, M. R. Aggregation Kinetics of Colloidal Particles Measured by Gas-Phase Differential Mobility Analysis. *Langmuir* **2009**, *25*, 140–146.

(26) Nishida, N.; Hara, M.; Sasabe, H.; Knoll, W. Formation and Exchange Processes of Alkanethiol Self-Assembled Monolayer on Au(111) Studied by Thermal Desorption Spectroscopy and Scanning Tunneling Microscopy. *Jpn. J. Appl. Phys. 1* **1997**, *36*, 2379–2385.

(27) Nishida, N.; Hara, M.; Sasabe, H.; Knoll, W. Thermal Desorption Spectroscopy of Alkanethiol Self-Assembled Monolayer on Au(111). *Jpn. J. Appl. Phys. 1* **1996**, *35*, 5866–5872.

(28) Tsai, D. H.; Zangmeister, R. A.; Pease Iii, L. F.; Tarlov, M. J.; Zachariah, M. R. Gas-Phase Ion-Mobility Characterization of SAM-Functionalized Au Nanoparticles. *Langmuir* **2008**, *24*, 8483–8490.

(29) Jokerst, J. V.; Lobovkina, T.; Zare, R. N.; Gambhir, S. S. Nanoparticle PEGylation for Imaging and Therapy. *Nanomedicine-UK* **2011**, *6*, 715–728.

(30) Tsai, D. H.; Davila-Morris, M.; DelRio, F. W.; Guha, S.; Zachariah, M. R.; Hackley, V. A. Quantitative Determination of Competitive Molecular Adsorption on Gold Nanoparticles Using Attenuated Total Reflectance-Fourier Transform Infrared Spectroscopy. *Langmuir* **2011**, *27*, 9302–9313.

(31) Tsai, D. H.; DelRio, F. W.; MacCuspie, R. I.; Cho, T. J.; Zachariah, M. R.; Hackley, V. A. Competitive Adsorption of Thiolated Polyethylene Glycol and Mercaptopropionic Acid on Gold Nanoparticles Measured by Physical Characterization Methods. *Langmuir* **2010**, *26*, 10325–10333.

(32) Tsai, D. H.; Elzey, S.; DelRio, F. W.; Keene, A. M.; Tyner, K. M.; Clogston, J. D.; MacCuspie, R. I.; Guha, S.; Zachariah, M. R.; Hackley, V. A. Tumor Necrosis Factor Interaction with Gold Nanoparticles. *Nanoscale* **2012**, *4*, 3208–3217.

(33) Pease, L. F.; Tsai, D. H.; Hertz, J. L.; Zangmeister, R. A.; Zachariah, M. R.; Tarlov, M. J. Packing and Size Determination of Colloidal Nanoclusters. *Langmuir* **2010**, *26*, 11384–11390.

(34) Cho, T. J.; Hackley, V. A. Fractionation and Characterization of Gold Nanoparticles in Aqueous Solution: Asymmetric-Flow Field Flow Fractionation with MALS, DLS, and UV-Vis Detection. *Anal. Bioanal. Chem.* **2010**, *398*, 2003–2018.

(35) Tsai, D. H.; Cho, T. J.; Elzey, S. R.; Gigault, J. C.; Hackley, V. A. Quantitative Analysis of Dendron-Conjugated Cisplatin-Complexed Gold Nanoparticles Using Scanning Particle Mobility Mass Spectrometry. *Nanoscale* **2013**, *5*, 5390–5395.

(36) Elzey, S.; Tsai, D. H.; Yu, L. L.; Winchester, M. R.; Kelley, M. E.; Hackley, V. A. Real-Time Size Discrimination and Elemental Analysis of Gold Nanoparticles Using ES-DMA Coupled to ICP-MS. *Anal. Bioanal. Chem.* **2013**, *405*, 2279–2288.

(37) Moulder, J. F.; Stickle, W. F.; Sobol, P. E.; Bomben, K. D. *Handbook of X-ray Photoelectron Spectroscopy*; Perkin-Elmer Corp: Eden Prairie, MN, 1995.

(38) Hunter, R. J. *Zeta Potential in Colloid Science*; Academic Press: San Diego, CA, 1988.

(39) Weisbecker, C. S.; Merritt, M. V.; Whitesides, G. M. Molecular Self-Assembly of Aliphatic Thiols on Gold Colloids. *Langmuir* **1996**, *12*, 3763–3772.

(40) Hinds, W. C. *Aerosol Technology: Properties, Behavior, and Measurement of Airborne Particles*; 2nd ed.; John Wiley & Sons: New York, 1999.

(41) Russel, W. B.; Saville, D. A.; Schowalter, W. R. *Colloidal Dispersions*; Cambridge University Press: New York, 1989.

(42) Hinterwirth, H.; Kappel, S.; Waitz, T.; Prohaska, T.; Lindner, W.; Lammerhofer, M. Quantifying Thiol Ligand Density of Self-Assembled Monolayers on Gold Nanoparticles by Inductively Coupled Plasma-Mass Spectrometry. *ACS Nano* **2013**, *7*, 1129–1136.

(43) Gorham, J.; Smith, B.; Fairbrother, D. H. Modification of Alkanethiolate Self-Assembled Monolayers by Atomic Hydrogen: Influence of Alkyl Chain Length. *J. Phys. Chem. C* **2007**, *111*, 374–382.

(44) Mikhlin, Y.; Likhatski, M.; Tomashevich, Y.; Romanchenko, A.; Erenburg, S.; Trubina, S. XAS and XPS Examination of the Au–S Nanostructures Produced via the Reduction of Aqueous Gold(Iii) By Sulfide Ions. *J. Electron Spectrosc.* **2010**, *177*, 24–29.

(45) Schulz, F.; Vossmeyer, T.; Bastus, N. G.; Weller, H. Effect of the Spacer Structure on the Stability of Gold Nanoparticles Functionalized with Monodentate Thiolated Poly(ethylene glycol) Ligands. *Langmuir* **2013**, *29*, 9897–9908.

(46) Stewart, M. H.; Susumu, K.; Mei, B. C.; Medintz, I. L.; Delehanty, J. B.; Blanco-Canosa, J. B.; Dawson, P. E.; Mattoussi, H. Multidentate Poly(ethylene glycol) Ligands Provide Colloidal Stability to Semiconductor and Metallic Nanocrystals in Extreme Conditions. *J. Am. Chem. Soc.* **2010**, *132*, 9804–9813.